Advanced Functional Materials

ADVANCED FUNCTIONAL MATERIALS
www.afm-journal.de

RESEARCH ARTICLE OPEN ACCESS

A Bioresorbable Neural Interface for On-Demand Thermal Pain Block

Jeonghwan Park[1,2] | Hak-Young Ahn[1,2] | Minho Seong[3] | Taehoon Kim[1,2] | Yulin Zhou[4] | Yameng Xu[5,12] | Jaehee Lee[1,2] | Ritika Raj Menghani[4] | Yujin Choi[1,2] | Minsu Park[6] | Nadir Muzaffar[7] | Youngeun Lee[8] | Seung Gi Seo[1,2] | Jong Uk Kim[1,2] | Sang Min Won[9] | Jahyun Koo[10] | Elena Aprea[11] | Taeyeon Kim[1,2] | Ying Yan[12] | Matthew R. MacEwan[12] | Wilson Z. Ray[12] | Raudel Avila[4] | Geumbee Lee[13] | John A. Rogers[1,2,7,14]

[1]Querrey Simpson Institute For Bioelectronics, Northwestern University, Evanston, Illinois, USA | [2]Center For Bio-Integrated Electronics, Northwestern University, Evanston, Illinois, USA | [3]Department of Fire Protection Engineering, Pukyong National University, Busan, Republic of Korea | [4]Department of Mechanical Engineering, Rice University, Houston, Texas, USA | [5]Institute of Materials Science and Engineering, Washington University in St. Louis, St. Louis, Missouri, USA | [6]Department of Polymer Science and Engineering, Dankook University, Yongin, Republic of Korea | [7]Department of Materials Science and Engineering, Northwestern University, Evanston, Illinois, USA | [8]Department of Materials Science and Engineering, Yonsei University, Seoul, Republic of Korea | [9]Department of Electrical and Computer Engineering, Sungkyunkwan University, Suwon, Republic of Korea | [10]School of Biomedical Engineering, Interdisciplinary Program in Precision Public Health, Korea University, Seoul, Republic of Korea | [11]Department of Microelectronics, Delft University of Technology, CD Delft, Netherlands | [12]Department of Neurosurgery, Washington University School of Medicine in St. Louis, St. Louis, Missouri, USA | [13]Department of Chemical Engineering, School of Chemical Engineering and Applied Chemistry, Kyungpook National University, Daegu, Republic of Korea | [14]Department of Biomedical Engineering, Department of Mechanical Engineering, Department of Neurological Surgery, Northwestern University, Evanston, Illinois, USA

Correspondence: Raudel Avila (ra88@rice.edu) | Geumbee Lee (geumbee.lee@knu.ac.kr) | John A. Rogers (jrogers@northwestern.edu)

Received: 8 November 2025 | **Revised:** 4 December 2025 | **Accepted:** 9 December 2025

Keywords: bioresorbable neural interface | soft biodegradable polymers | thermal neuromodulation | pain management | wireless power transfer

ABSTRACT

Conventional strategies for the management of acute pain have significant limitations. Pharmaceutical approaches carry risks for addiction and misuse. Standard implantable devices require secondary surgeries for removal and physical tethers to external systems for power and control. Recent work on bioresorbable electrical stimulators overcomes certain of these drawbacks, but existing versions still depend on transcutaneous leads. Here, we introduce a platform that employs thermal mechanisms for nerve block to bypass some of these limitations. The system integrates both a Joule heating element and a resistive temperature sensor in a soft cuff structure as a nerve interface, in which most of the materials are bioresorbable over a clinically relevant timeframe. This design enables precise control of nerve temperature within a safe range (≤45°C) for effective nerve block through a feedback-guided strategy that continuously monitors temperature and adjusts current in real time. Options for wireless power delivery eliminate the need for external interfaces. Small animal model studies confirm the reversible and non-invasive operation of this system. The results demonstrate effective suppression of compound nerve action potentials in response to thermal stimulation, with recovery of nerve conduction upon cooling. These findings highlight the potential of this platform as a safe and effective solution to acute pain management.

1 | Introduction

Peripheral neuropathic pain that arises from surgical trauma, metabolic disorders, physical nerve injury or other sources, remains a complex and persistent challenge in clinical practice [1]. While opioids serve as a standard pharmacological treatment approach, they suffer from systemic toxicity, rapid tolerance development, and a high potential for addiction [2, 3]. These limitations create interest in non-pharmacological schemes that offer localized, reversible modulation of pain signaling, in adjustable formats that address patient-specific needs [4–6].

Non-pharmacological adjunctive strategies such as transcutaneous and percutaneous electrical nerve stimulation (TENS and PENS) deliver targeted electrical stimulation to peripheral nerves to suppress pain signaling in a non-invasive or minimally invasive manner [7–9]. These methods enable reversible modulation of nerve activity and can block pain signals within milliseconds; however, their superficial engagement with peripheral nerves, variability in electrode placement, and challenges with patient compliance restrict their effectiveness. Direct neural interfaces that form conformal contact with nerves address certain of these drawbacks through delivery of electrical stimulation in a uniform and stable manner [10, 11]. Both precision and reliability extend operation across a broader clinical window, ranging from acute postoperative episodes to prolonged neuropathic conditions [12–14]. Nevertheless, clinical translation of such technologies faces challenges. First, most existing devices rely on permanent, non-degradable materials that often necessitate secondary retrieval procedures and associated complications due to chronic inflammation and fibrosis [15, 16]. Second, current systems lack real-time sensing capabilities for closed-loop control. Third, power delivery architectures often rely on transcutaneous leads, and associated risks for infection and limits in patient mobility [17, 18]. These deficiencies motivate interest in alternative technologies.

Bioresorbable electronics as the basis for temporary implants in this context offer some promise. By exploiting materials that naturally resorb within the body after a therapeutic timeframe, such platforms mitigate long-term complications and eliminate the surgical burden associated with device retrieval [19–22]. When integrated with wireless power transfer, they may further enable non-invasive and on-demand operation, allowing neuromodulation to be activated or deactivated dynamically in alignment with patient-specific needs and without risks and drawbacks associated with transcutaneous leads. These features align well with clinical scenarios that demand temporary yet precisely timed interventions, such as those to address postoperative pain or acute neuropathic episodes [13, 14, 23, 24]. Within this emerging paradigm, engineering strategies for neuromodulation span electrical, optical, and thermal domains, each with distinct mechanisms of action and translational barriers. Electrical stimulation delivers controlled current pulses that depolarize or hyperpolarize neuronal membranes. At kilohertz frequencies, alternating currents can produce reversible conduction block [25, 26], but these systems, in current engineering versions, require tethered power sources and transcutaneous leads to cuff electrodes that often suffer from accelerated electrochemical degradation during operation [27]. Optogenetic methods activate genetically introduced, light-sensitive ion channels with millisecond precision, yet translation remains limited by the requirement for genetic modification and the absence of resorbable light sources. Combining implantable, bioresorbable fibers with external light sources (e.g., lasers) represents an option, but the necessary tethered configuration is a significant drawback [28–33]. Thermal neuromodulation (e.g., cooling- and heating-based) offers unique benefits in this context. Heat conduction through biocompatible, electrically insulating materials enables fully encapsulated, inflammation-resistant device designs [34, 35]. Cooling decreases nerve conduction velocity by slowing ion channel kinetics, which can transiently suppress action potential transmission. Integrated temperature sensors provide an ability to regulate the cooling to reach desired temperatures, with robust closed-loop control. The technical requirements for this cooling demand, however, complex and tethered architectures such as those that use the flow of cooling fluids through implanted microfluidic channels [36, 37]. Heating, in contrast, elevates local temperature to a threshold that disrupts normal depolarization, thereby producing a reversible block of signal conduction. Heating can be induced locally through Joule heating, in simple device designs that can readily establish soft, conformal contacts with neural tissues [38–40]. Existing systems of this type rely, however, on permanent configurations, wired and non-bioresorbable materials, raising concerns about their clinical adoption and the need for surgical removal [41, 42]. A bioresorbable neural interface capable of delivering wireless, on-demand thermal modulation with integrated sensing for precise control therefore represents an attractive solution.

Here, we introduce bioresorbable, implantable neural electronic system that is capable of on-demand, spatially precise thermal nerve block. This platform integrates a microscale thermal actuator (i.e., a resistive heater) and thermistor (i.e., a temperature sensor) into a bioresorbable polymeric substrate. Localized heating induces a reversible conduction block, while an integrated temperature regulation system ensures precise thermal control to prevent overheating by leveraging real-time sensor feedback to dynamically adjust the input current for stable operation to a temperature setpoint. As a substrate and encapsulating layer, the structure incorporates either polyanhydride (PA) with tunable chemical composition or plasticized regenerated silk fibroin (p-RSF) with tunable crystallinity. Both options provide mechanical flexibility and controlled degradation over clinically relevant timescales. In a rat sciatic nerve model, the device achieves effective and reversible suppression of compound nerve action potentials (CNAPs) and supports recovery of nerve conduction after cooling. Demonstrations of wireless power transfer to support operation suggest the ability to avoid the need for transcutaneous interfaces. The result is a nonpharmacological, minimally invasive, electronic platform for advanced pain management.

2 | Results and Discussion

2.1 | Materials and Device Design Features

Conventional approaches for pain treatment primarily rely on (i) pharmacological therapy (e.g., opioids) and (ii) electrical stimulation (e.g., TENS, PENS) (Figure 1a-i) [19]. The approach

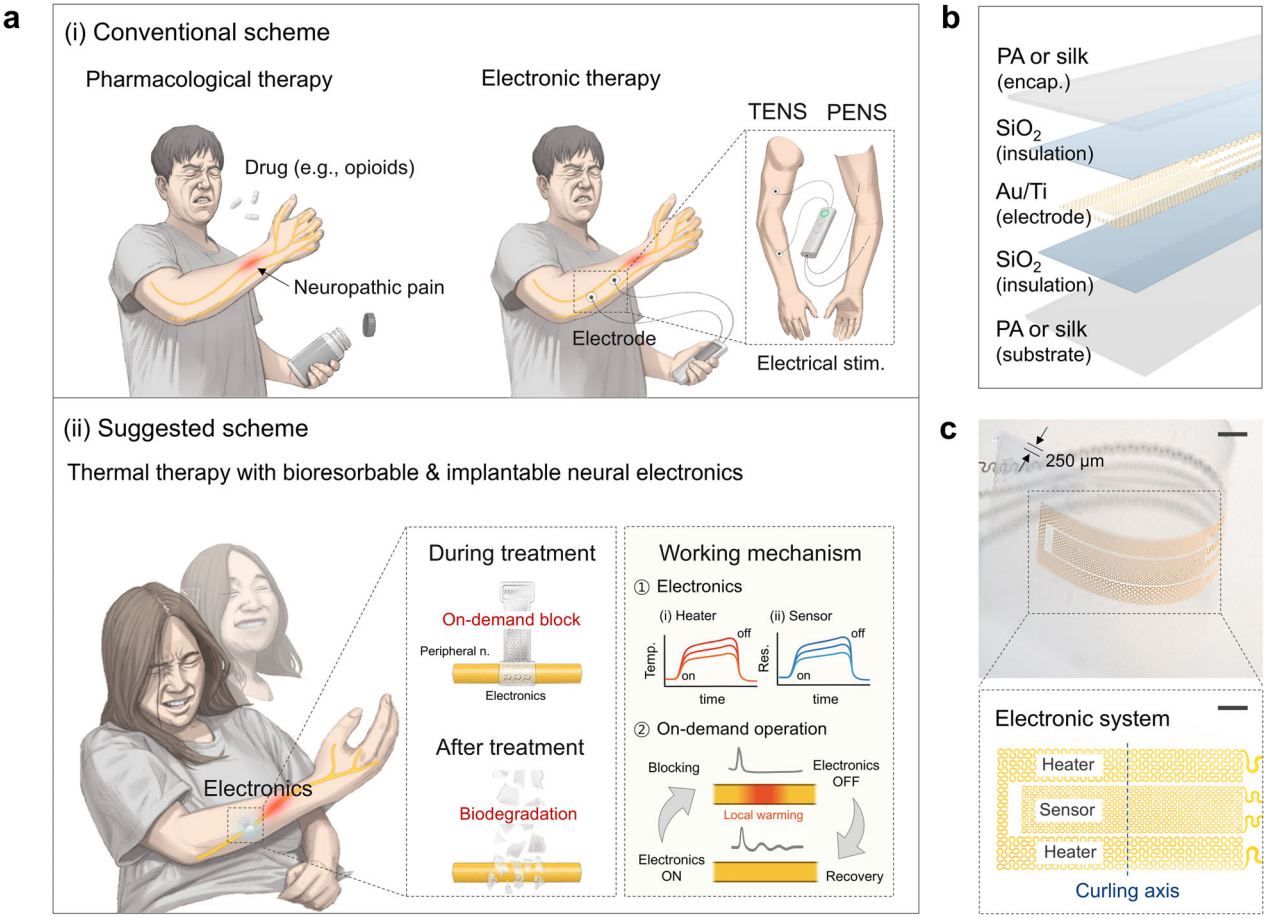

FIGURE 1 | Illustrations of schemes for acute pain mitigation and design features of an implantable, bioresorbable platform for thermal nerve block. a) Conceptual illustrations of (i) conventional pain management approaches and (ii) the approach presented here. b) Exploded view illustration of the layered device layout. c) Picture and diagram of the device, highlighting the serpentine traces that define the heating and sensing elements. Scale bars, 1 mm.

introduced here offers an alternative, based on thermal neuromodulation using an implantable platform with integrated sensing functionality. The system allows for precise control of heating, in a construct that is largely bioresorbable, to eliminate the need for surgical retrieval after a clinically relevant period of operation (Figure 1a-ii).

Figure 1b presents an exploded-view illustration of the device, which consists of (i) thin metal traces in a serpentine geometry (gold, Au; 120 nm thick) to define structures for Joule heating and resistive temperature sensing, (ii) an inorganic dielectric layer (silicon dioxide, SiO_2; 500 nm thick) positioned at the neutral mechanical plane to ensure both mechanical stability and electrical insulation, and (iii) thin layers of bioresorbable polymers (125 μm-thick PA for short-term application; 6 μm-thick p-RSF for long-term application) on the top and bottom to isolate the active parts of the device from biofluids over timescales of interest. Detailed device fabrication procedures are available in Figure S1 and in Experimental Section/Methods. An additional option is in components to support wireless power transfer, as described subsequently.

The thin geometry of the polymeric encapsulation (elastic modulus ~2.5 MPa for PA; ~150 MPa for p-RSF) allows the device to wrap peripheral nerves (average diameter, 1–2 mm) in a manner that ensures effective thermal coupling, while minimizing tissue damage during implantation and subsequent use (Figure 1c) [43]. Photocuring the PA enables fabrication of tubular cuffs in a molding process (Figure S2) that defines a diameter to match the geometry of a targeted nerve.

All constituent materials are either resorbable (i.e., PA, p-RSF, SiO_2) or biocompatible (i.e., Au). Au provides stable and predictable electrical performance under physiological conditions, owing to its high conductivity and exceptional chemical stability, which supports consistent operation of the thermal elements in this system. Extensive use and well-established biocompatibility in neural interfaces further justify its selection as the electrical layer for this platform [11, 44, 45]. In addition, the total amount of Au used in our device is small (113.7 μg in mass), corresponding to only 0.13% and 3.85% of the total device weight for the PA-based and p-RSF-based platforms, respectively (Table S1). The resorption of the relatively thick polymeric encapsulation layers defines the functional lifetime. The PA material undergoes hydrolysis within a period of days, depending on the polymer composition [37]. The formulation of PA used here has a dissolution rate of ≈ 1.3 μm d^{-1} [46], primarily driven by hydrolysis of ester groups within the polymer chains. RSF is a biocompatible

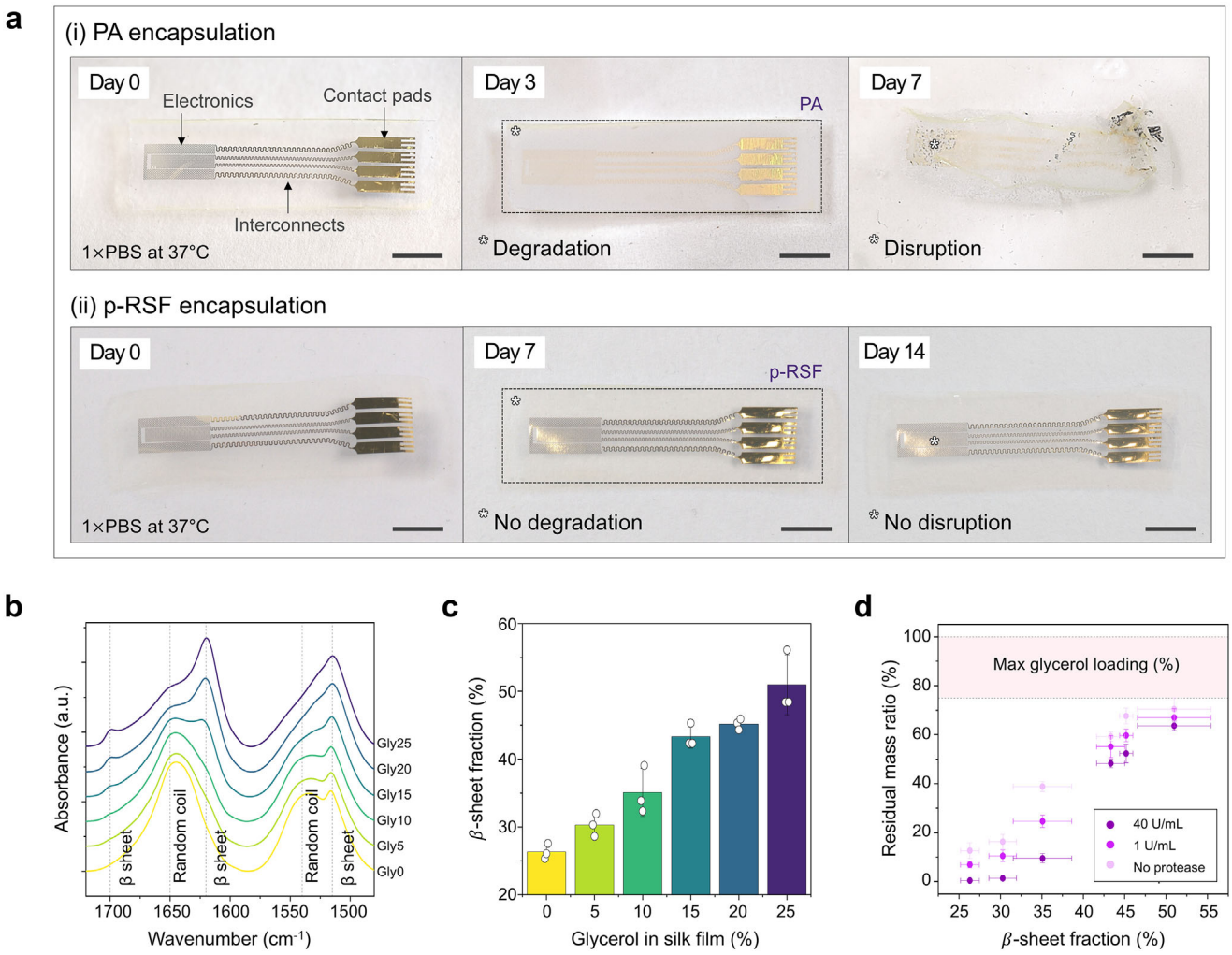

FIGURE 2 | Time-dependent structural degradation of PA- and p-RSF-encapsulated devices under physiological conditions. a) Sequence of images showing the dissolution of the (i) PA-encapsulated and (ii) p-RSF-encapsulated devices at different times following immersion in 1 × PBS at physiological condition (pH 7.4, 37°C). Scale bars, 5 mm. b) FT-IR spectra of RSF films with varying glycerol contents (0%–25% by silk mass). c) Quantification of β-sheet content as a function of glycerol loading (%). Dots, data points ($n = 3$); error bars, mean ± s.d. d) Residual mass ratio (%) of RSF-encapsulated devices with varying β-sheet content after 14-day incubation in 1×PBS and protease-containing 1×PBS. Dots, data points ($n = 4$); error bars, mean ± s.d.

and biodegradable natural polymer extensively employed in non-electronic implantable systems [47–50], with several that have U.S. Food and Drug Administration (FDA) clearance [51]. Bioresorption proceeds primarily through enzymatic cleavage of peptide bonds, typically accelerated by proteases present in vivo, and strongly influenced by local physiological conditions (e.g., protease activity, pH, temperature) and the β-sheet crystallinity of the film. The dissolution kinetics of SiO_2 interlayer depend on the deposition or growth method (SiO_2 $(s) + 2H_2O$ $(l) \rightarrow Si(OH)_4$ (aq); dissolution rate, 0.005–10 nm d^{-1}) [52–54].

Figure 2a compares time-dependent degradation behavior of PA- and p-RSF-encapsulated devices immersed in 1 × PBS (pH 7.4) at physiological temperature. Although many bioresorbable substrates appear in medical devices, PA and p-RSF offer clear advantages through their surface-erosion behavior (Table S2, Supporting Information). In contrast to bulk-eroding polymers, these materials erode from the surface with minimal swelling and maintain stable mechanical support for thin-film metal traces during operation [54, 55]. PA undergoes dissolution primarily within a week, leading to disruption and fragmentation of Au traces and the SiO_2 layers, due to mechanical failure rather than chemical dissolution (Figure 2a-i). In contrast, the p-RSF-encapsulated platform (β-sheet crystallinity, ~50%) remains intact even after 14 days due to the densely packed β-sheet crystalline domains (Figure 2a-ii), thereby serving as a viable alternative encapsulation material for long-term biocompatible nerve-block applications [56–58]. As a result, the PA-encapsulated device maintains 92% of its initial resistance by day 3, but fails after day 5 while the p-RSF-encapsulated device exhibits stable resistance throughout 14 days, as summarized in Figure S3, consistent with observations in Figure 2a.

By modulating hydrogen bonding and promoting β-sheet formation (Figure S4) [59–63], glycerol loading influences both the conformational and mechanical characteristics of RSF [63–65]. As a plasticizer, glycerol partially disrupts or reorganizes intermolecular hydrogen-bond networks, increasing chain mobility and thereby reducing brittleness while enhancing

flexibility in the resulting films. These effects enable p-RSF overcomes the brittleness and rapid dissolution of pure silk (Figure S5) and, importantly, conforms around small-diameter objects with reduced contact pressure (Figure S6). These features collectively establish p-RSF as a promising encapsulation layer for bioresorbable neural interfaces. Notably, FT-IR spectra reveal a progressive transition from random coil/α-helix to β-sheet conformations with increasing glycerol content, accompanied by a near-linear rise in β-sheet fraction (Figure 2b,c; Figure S7).

The β-sheet fraction governs the degradation of p-RSF, where higher-crystallinity films degrade more slowly under PBS and protease-rich conditions while low-crystallinity films (<35%) disintegrate within 14 days (Figure 2d; Figures S8–S10). This tunable degradation behavior imparts both mechanical resilience and controlled bioresorption, making p-RSF suitable for long-term neural interfaces.

2.2 | Thermal and Mechanical Properties

An in vitro analysis setup reveals the performance under settings that mimic the neural tissue environment. The model uses a silicone tube (inner diameter, 1.5 mm) filled with 1 × PBS (pH 7.4) at 37°C for a peripheral nerve and a surrounding matrix of agar-based hydrogel (modulus, 60 kPa; thermal conductivity, 0.5–0.6 W m^{-1} K^{-1}) for soft biological tissues (Figure 3a) [36, 66, 67]. A bath maintains a constant target temperature (≈37°C) to replicate physiological conditions and ensure consistent thermal measurements (Figure S11 and Experimental Section).

Current applied to the Joule heating element of the device leads to a heating at rates that depend on the magnitude of the current (e.g., 0.24–1.36°C s^{-1} for input current $I_{input,}$ 15–45 mA) (Figure 3b; Figure S12). As a specific example, at 25 mA, the device reaches a temperature of ~42°C within 30 s and maintains a stable localized temperature of 43.5°C ± 0.3°C, remaining below the upper temperature threshold (≤45°C) throughout to ensure tissue safety [34, 68, 69]. Upon termination of the current, the temperature returns to baseline (i.e., physiological temperature, 37°C) within 3 min. Figure 3c presents the simultaneous operation of the heating and the sensing elements under stepwise increases and decreases in input current. The response demonstrates reversible behavior without hysteresis.

The integrated Au thermistor relies on the temperature coefficient of resistance (measured as 0.0036°C^{-1}, consistent with literature values [70]) and exhibits linear behavior across the relevant temperature range (Figure 3d). This component allows local temperature monitoring during operation by reading resistance changes with temperature, enabling active feedback control (Figure 3e). Operation in this manner is important to stabilize thermal actuation at a precisely targeted threshold to achieve a block without tissue damage. Demonstrations involve precise control under various ambient conditions established within a hydrogel phantom setup (Figure 3f; Figure S13). As the surrounding temperature increases from 30°C to 40°C, the thermistor yields temperature readings for real-time feedback. The system thus responds by decreasing the current in this case from 36 mA to 19 mA, thereby sustaining the target heater temperature near 44°C–45°C. Further investigations confirm that the feedback principle protects against overheating (>45°C) scenarios (Figure S14).

The results of finite element analysis (FEA) under the same conditions align with the experimental measurements (Figure 3g). Three-dimensional thermal maps obtained from the FEA models track the progression of heat propagation over time in the PA-encapsulation and the nerve (Figure 3h). At 30 s post-stimulation, heat remains concentrated near the heater core, with gradual lateral and inward diffusion along the nerve. By 90 s, the heating zone extends across both the nerve surface and core, with spatial asymmetries that reflect the contact with the nerve. Temperatures in these regions reach a spatially uniform value sufficient for reversible nerve block (42–45°C), while remaining below the damage threshold of 45°C [34, 68, 69]. These simulations indicate that the heating is largely confined to the nerve.

Practical applications also require stable mechanical characteristics during motions that can occur at the locations of peripheral nerves. Figure 4 summarizes measurements of the mechanical stability of a device (width: 10 mm; length: 30 mm; thickness: 0.25 mm; weight: 110 mg) under expected physiologically relevant deformations. During bending (radius of curvature: 1.5 mm, comparable to the rat sciatic nerve) and twisting (45°), FEA quantifies the distribution of strains in the device and experimental measurements capture the deformations (Figure 4a). For these cases, the maximum strains in the Au remain below the yield threshold of 0.3% (Figure 4b). Infrared (IR) thermal images indicate consistent heating profiles before and after bending and twisting (Figure 4c).

During compression-induced bending (curvature range: 0.01–1 mm^{-1}) and high-cycle mechanical loading (curvature: 0.1 mm^{-1}; 10 mm s^{-1} buckling rate, 20,000 cycles), the changes in resistance ($\Delta R/R_0$) in the Au traces remain within ±0.001 (Figure 4d). Even under extreme mechanical torsion, including twisting from −30° to +30° and repetitive cycles of 30° at 30° s^{-1} for 20,000 cycles, the resistance variation remains within ±0.002 (Figure 4e). These values agree with the theoretical calculation (see Experimental Section/Methods) and with prior studies on nanometer-thick films exhibiting elastic deformation [71, 72]

2.3 | In Vivo Demonstration of Thermally Induced, Reversible Nerve Block

Acute studies using animal models involve implantation of PA-based devices (see Figure 1 section on device exploded view for layer thickness and composition) interfaced to the sciatic nerve. The device for an acute model is composed of biodegradable and biocompatible materials. Even for long-term implantation in chronic models, extensive prior studies on materials of p-RSF and Au secure in vivo stability to p-RSF-encapsulated devices [11, 57, 58, 73]. Surgical procedures involve exposing the nerve via dorsal gluteal muscle incision, to allow implantation of three components: a stimulating electrode, the device, and a recording electrode (Figure 5a,b). The first of these three consists of a bipolar, stimulating hook electrode (300 μm diameter, 1 mm interspace) that wraps around the proximal sciatic nerve for delivery of electrical pulses to activate neurons, including motor and sensory pathways. These stimuli mimic nociceptive action

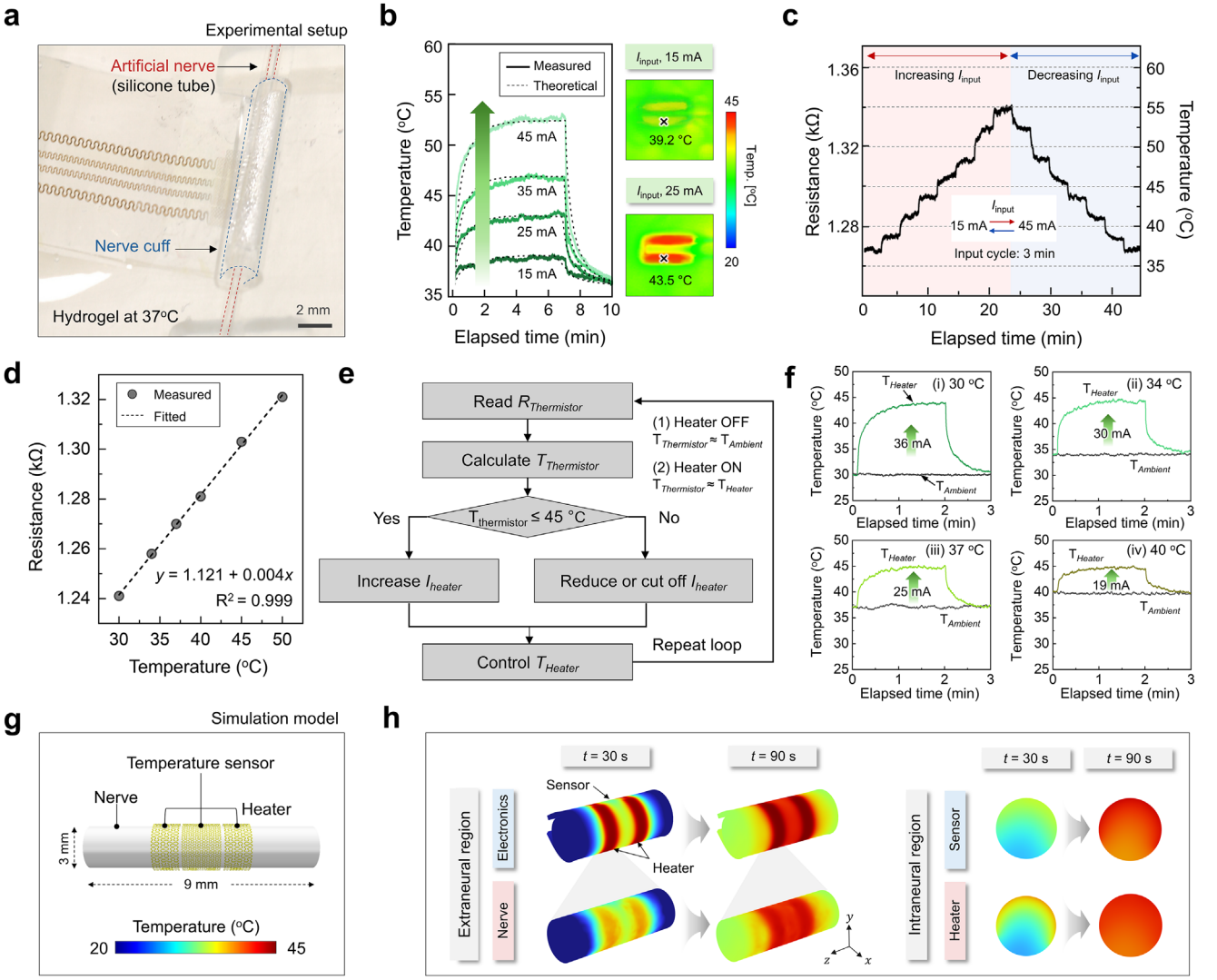

FIGURE 3 | Measurements and simulations of the thermal and electrical properties. a) Schematic illustration and optical image of the in vitro experimental setup for evaluating the thermal effects. b) Time-dependent temperature response, measured (solid line) and simulated (dashed line) of the device under thermal actuation with varying input currents (I_{input}, 15–45 mA), demonstrating stepwise heating behavior (left); and infrared (IR) thermal images (right) of the device showing localized heat distribution under in vitro phantom conditions (hydrogel, 37°C). c) Heating and cooling cycle analysis, displaying temperature variations over time for different I_{input} values under 37°C hydrogel conditions. d) Temperature-sensing characterization of the device as a thermistor, showing the changes in resistance with temperature under in vitro hydrogel conditions. e) Operational diagram of the closed-loop thermal regulation system. f) Active input current control which enables closed-loop regulation to achieve the safety threshold temperature (≤45°C) by detecting the ambient temperature under hydrogel conditions. g) Schematic illustration of the phantom model used in the simulation. h) Simulation results of thermal distribution in a nerve wrapped with the device at different time points (t = 30 s and t = 90 s), showing both surface and cross-sectional thermal maps. (left) Localized heating beneath the device along the nerve length; (right) spatial temperature gradients across the cross-section of the nerve under temperature sensor and heater.

potentials (amplitude, 1 mV; burst width, 0.3 s; 50 μs duration). The device locally warms the nerve to disrupt conduction. A bipolar recording cuff electrode (diameter, 500 μm; interspace, 1 mm) positioned at the distal sciatic nerve captures the resulting CNAP. During this process, the integrated temperature sensor continuously monitors local temperature (Figure 5c). Application of current to the heater raises the local temperature at a rate of ~0.3°C s^{-1}, reaching up to 45°C. As the current returns to zero, the temperature decreases to below 35 °C within 30 s [74, 75]

Sensory nerve block serves as a physical indicator of conduction suppression. The recording electrode, positioned on the peroneal nerve, a primarily sensory branch, enables quantitative analysis of CNAP amplitudes at the periphery (Figure 5d). Partial nerve block appears in 4 min after heater activation, and by 5 min, thermal accumulation induces a complete nerve block. Local heating in the range of 42–45°C defines the threshold for achieving a reversible thermal nerve block [34]. At this level, exposure on the order of a few minutes suppresses conduction without causing structural damage [34, 68, 69]. In contrast, prolonged heating (>30 min) above ~45°C leads to irreversible complete nerve block, as endothelial and axonal structures deteriorate progressively with increasing duration [34, 76–78]. To remain within the reversible window, the platform relies on intermittent

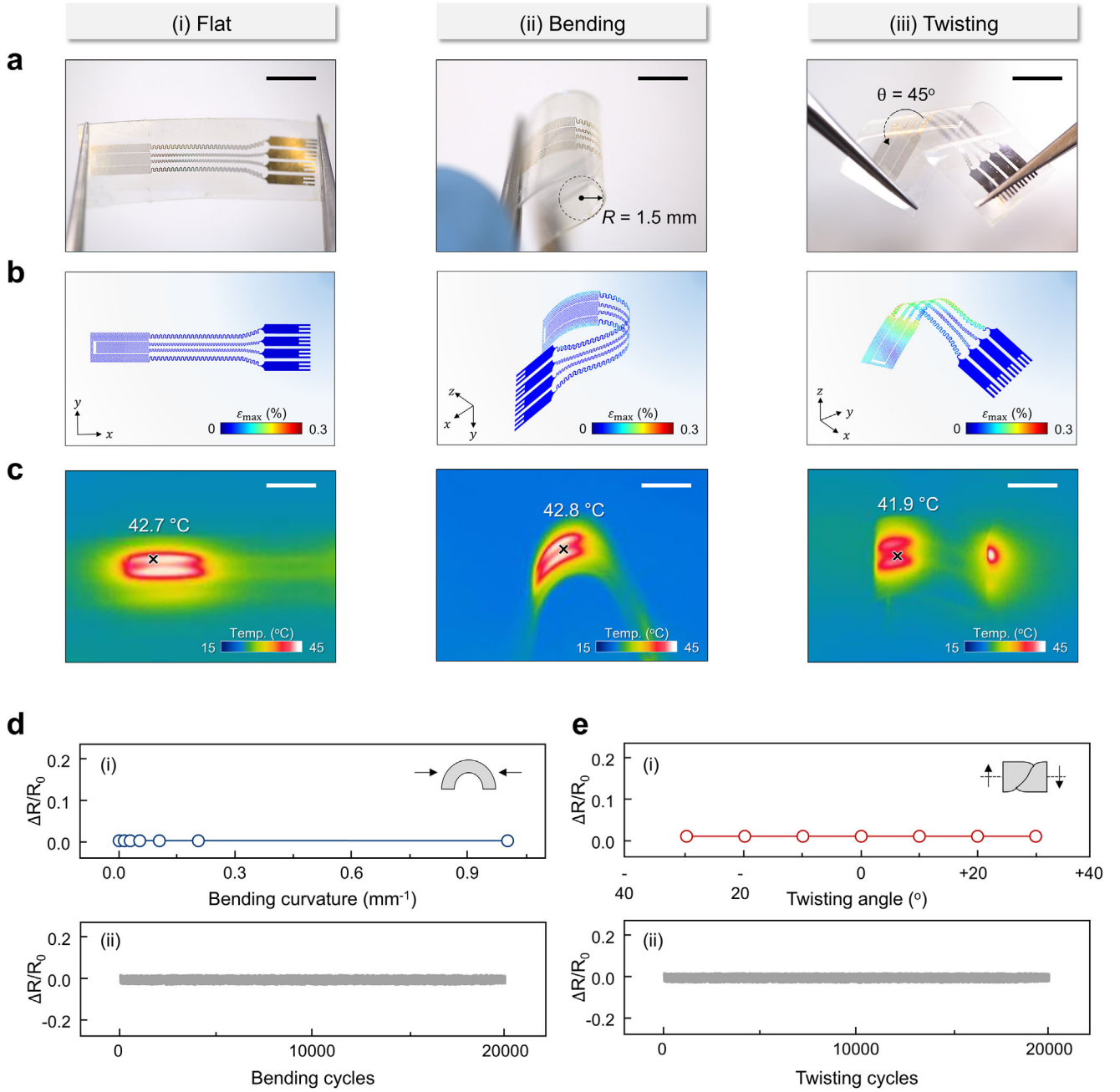

FIGURE 4 | Mechanical and electrical stability of the device under deformation. a) Optical images of the device under different mechanical states: (i) flat configuration, (ii) bending with a curvature radius of 1.5 mm, and (iii) twisting at a 45° angle. b) FEA results showing strain distribution under each deformation mode and maximum strain (ε_{max}). c) IR thermal images under the same mechanical conditions, showing stable temperature distribution. d) Changes in resistance of the device during bending (i) as a function of bending curvature (ranging from 0.01 to 1 mm^{-1}) and (ii) under cyclic bending (curvature of 0.1 mm^{-1}, loading rate of 10 mm s^{-1}, 20 000 cycles). e) Changes in resistance of the device during angular twisting (i) as a function of bending curvature (ranging from −30° to +30°) and (ii) during cyclic twisting (twisting of +30°, loading rate of 30° s^{-1}, 20 000 cycles). All scale bars, 5 mm.

cycles of heating and cooling. Specifically, the heater activates to raise the local temperature to 42–45°C within 5 min, coinciding with the transition from partial to complete block, and then deactivates. Passive cooling under ambient conditions restores the nerve temperature to a baseline value, such that conduction fully recovers, consistent with reversible operation (Figure 5d). Cycling between the block threshold and the injury threshold limits the cumulative temperature–time dose (consistent with CEM43 principles) [79, 80], thereby balancing efficacy with tissue safety for a reliable, damage-free nerve conduction block.

2.4 | Wireless Operation

Integration of a receiving (R_x) coil enables wireless power transfer through magnetic inductive coupling to an external radio

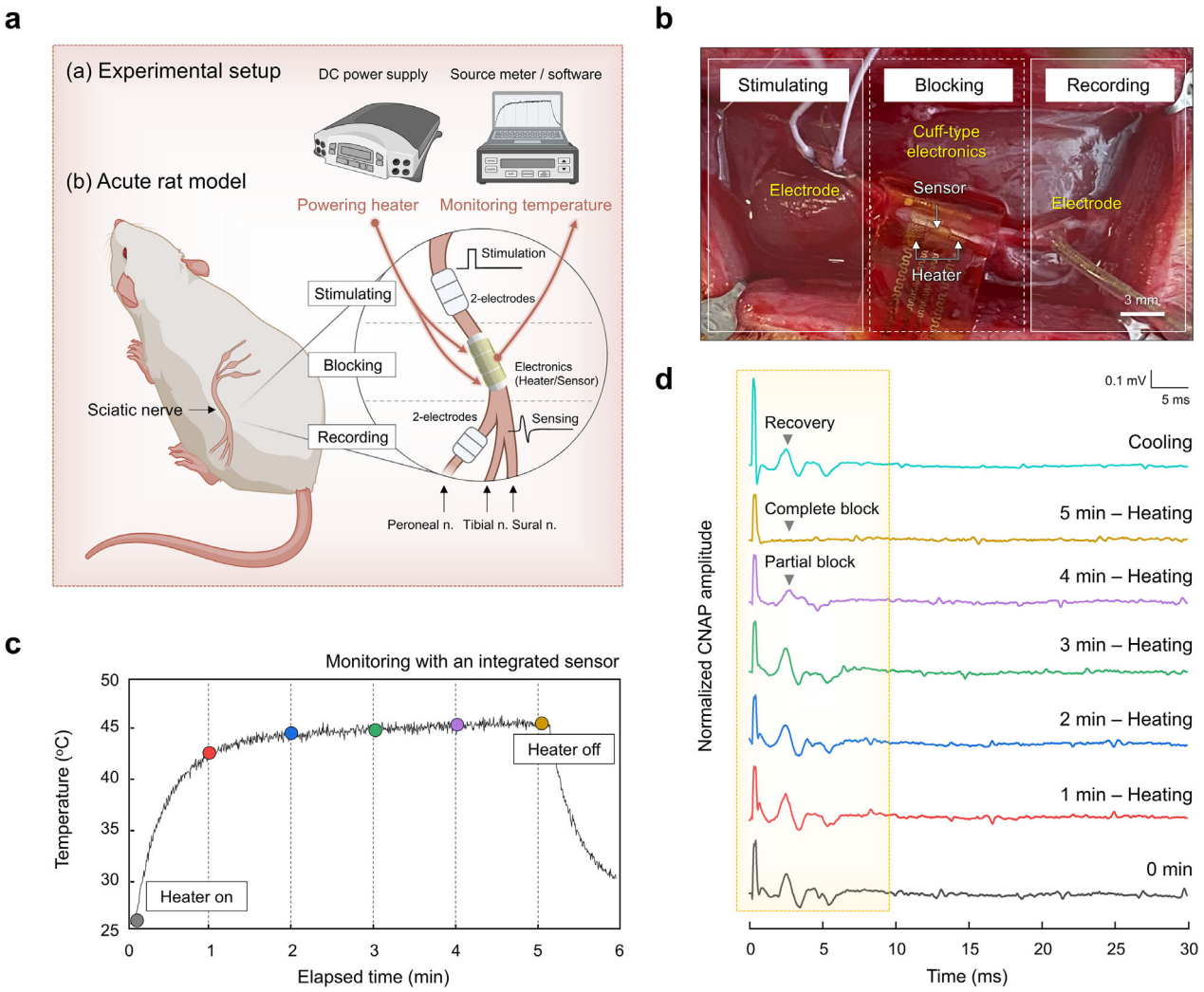

FIGURE 5 | In vivo evaluation of thermal nerve conduction block using the device. a) Schematic illustration of the implantation of the device in a rat model and the measurement setup. b) Optical image showing the placement of three components (i.e., stimulating electrode, device, and recording electrode) for acute in vivo physiological studies: a stimulating electrode placed on the sciatic nerve (left), the device positioned between the stimulating and recording electrodes (center), and a recording electrode placed on the peroneal nerve (right). c) Temperature profile monitored with the implanted sensor during thermal actuation of the heater. d) Changes in compound nerve action potential (CNAP) responses over the course of thermal accumulation.

frequency (RF) source operating in the high frequency range, at ~9.5 MHz in air and ~8.5 MHz in 1x PBS. (Figure 6a; Figure S15). The R_x coil employs transient, bioresorbable materials for all structural components and features a multilayer architecture with defined geometries (Figure 6b; Figure S16) [20]. Wireless operation allows heating to levels comparable to those of wired configurations described previously, to within a safety threshold (≤45°C) (Figure 6c) [34, 68, 69]. The experimental setup for wireless powering and thermal analysis operates under ambient conditions at 23°C (Figure S17). In this configuration, a transmitting (T_x) coil supplied with an RF power of 2.0 W at a frequency of 13.56 MHz and positioned at a spacing of 1 mm from the R_x coil leads to temperatures of 44°C ± 1°C (Figure 6c; Figure S18). Repetitive on/off cycling yields rapid, reproducible transitions between 42°C–45°C with 5 ± 0.5 s rise/decay, highlighting dynamic and on-demand thermal actuation (Figure 6d; Figure S17). IR thermal imaging directly confirms localized heating to a surface temperature of 43.9°C (Figure 6e) [34].

To assess the robustness of the wireless devices under realistic implantation-mimicking conditions, measurements quantify the output power delivered to a 1.2-kΩ load while the T_x–R_x separation distance (1–6 mm), lateral offset (0–50 mm), and angular misalignment (0–60°) vary (Figures S19–S21). The resulting datasets demonstrate that the system delivers sufficient power across subcutaneous-relevant depths and within positional variations expected in vivo. The overall trends corroborate prior studies on wireless biomedical devices and systems [20, 81–83], and the combined evidence defines the practical operation of the wireless link.

Advanced embodiments integrate a voltage-regulating diode that functions as a regulator to maintain a fixed operating voltage. Here, regulation becomes active once the input voltage (V_{in}) exceeds the regulating voltage (V_r). At voltages below V_r, regulation remains inactive and exerts minimal influence on the circuit, allowing the output voltage (V_{out}) to rise proportionally with V_{in}

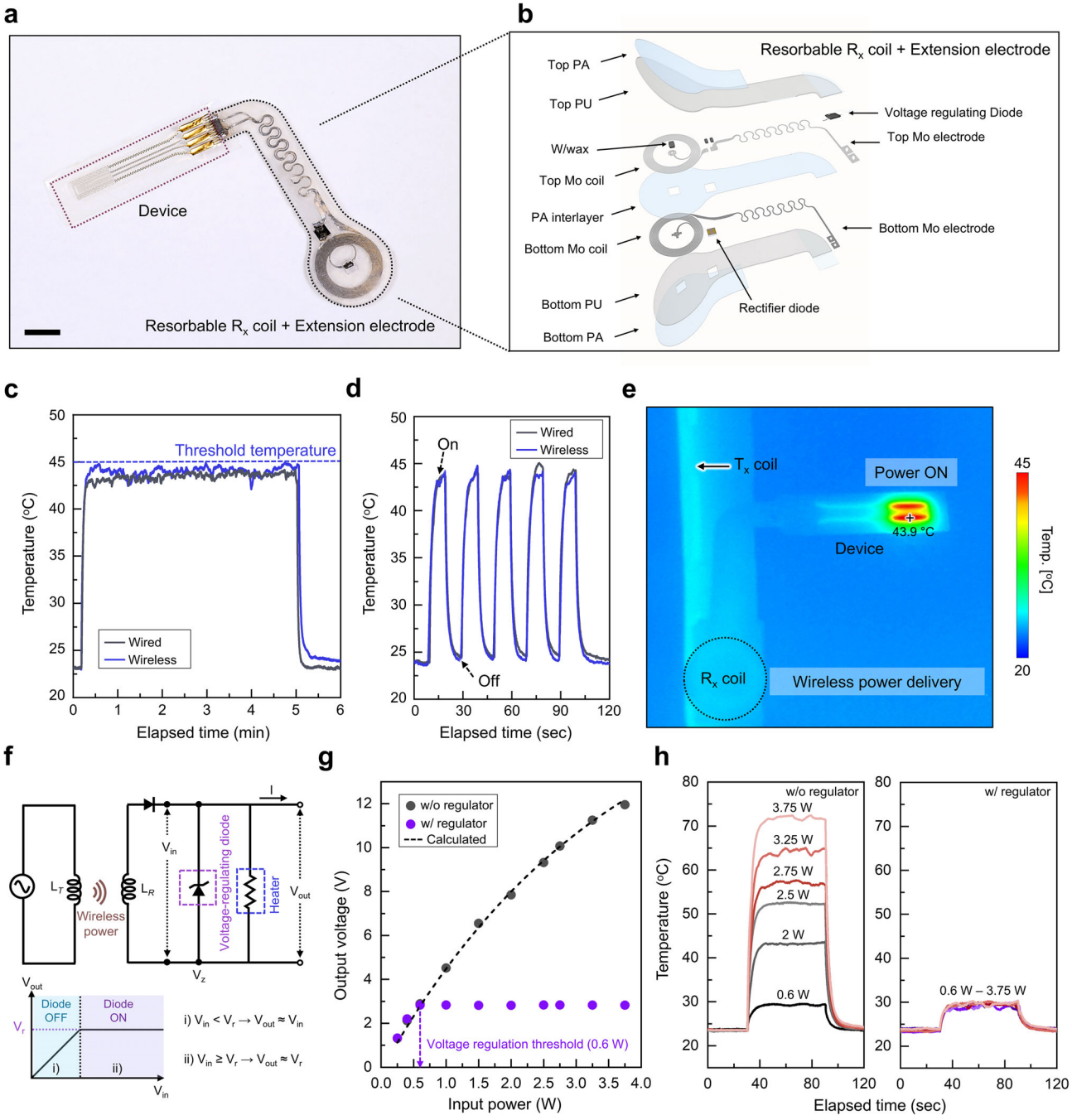

FIGURE 6 | Wireless operation. a) Optical image of the wireless system with an integrated resorbable R_x coil. Scale bar, 5 mm. b) Exploded view illustration of the R_x coil. c) Temperature profiles of wired and wireless modes of operation, showing consistent behavior in reaching and maintaining the threshold for thermal actuation. d) Repeated on–off heating cycles under both wired and wireless operation, demonstrating stable and reproducible thermal responses. e) IR thermal image showing localized heating of the device under wireless power delivery from the external T_x coil to R_x coil. f) Schematic illustration of the wireless system incorporating a voltage-regulating diode for controlled output delivery. g) Output voltage across the heater as a function of the input power to the T_x coil, with and without the regulator. h) Temperature profiles of the wireless device under different input powers (0.6–3.75 W) for the non-controlled (left) and voltage-controlled (right) systems.

(Figure 6f). This intrinsic regulation mechanism clamps the V_{out} above the activation threshold, ensuring consistent operation of the device. This voltage regulation directly translates into thermal stability during wireless operation. Absence of regulation exposes the tissue to risks of overheating. In the example reported here, the regulator clamps the output near 2.8 V beyond 0.6 W of input power, effectively limiting current flow and preventing thermal overload (Figure 6g). Correspondingly, the device temperature remains constant at ~28.5°C over the 0.6–3.75 W range, in sharp contrast to the unregulated condition where temperatures exceed 70°C (Figure 6h). Below the threshold, both conditions show comparable temperature responses (Figure S22). IR imaging provides direct confirmation of this stabilizing effect. Without voltage regulation, the device temperature rises to ~72.7°C at

3.75 W, whereas the regulated configuration maintains a uniform and safe temperature near 28.5°C under identical input conditions (Figure S23).

3 | Conclusion

This study presents a strategy for peripheral nerve conduction block that leverages precise thermal control to overcome the limitations of conventional implantable platforms. The design of the system integrates a thin-film metallic heater and temperature sensor on a biodegradable polymer substrate. This configuration enables both localized thermal neuromodulation for pain management and complete in vivo degradation without requiring secondary surgical removal. In vitro, in silico, and in vivo studies validate the functional performance and biocompatibility of the system. The developed platform features: (i) real-time feedback control through an integrated temperature sensor, (ii) mechanical flexibility supported by the polymeric substrate, and (iii) a combined material design comprising biocompatible metals and polymers with tunable degradation characteristics. In the rodent model, the device rapidly and effectively suppresses peripheral nerve conduction through localized heating and promptly recovers upon cessation of stimulation. This outcome demonstrates that thermal stimulation provides a simple yet effective and reversible mechanism for nerve block, addressing key limitations of conventional implantable electronics that rely on non-resorbable materials and necessitate surgical extraction. Additionally, real-time temperature monitoring minimizes the risk of overheating and supports safe, on-demand suppression of pain relief. Further options in wireless power delivery enable untethered operation, as an important aspect in practical use. This platform also enables a practical route for future translation into fully transient neural electronics by replacing the metallic traces with representative bioresorbable metals. This work suggests a class of electroceuticals based on localized thermal modulation for drug-free pain management, applicable to both postoperative acute pain and chronic, treatment-resistant conditions.

4 | Experimental Section

4.1 | Fabrication Procedures-Serpentine Thin-Film Metal Electrodes

Multilayer deposition and patterning processes define serpentine interconnects on silicon wafer substrates. Wet oxidation at 1050°C for 25 min forms a uniform SiO_2 layer on these wafers. Spin-coating a precursor to polyimide (PI, Sigma-Aldrich) at 5000 rpm for 1 min followed by a two-step soft bake at 95 °C for 30 s and 150°C for 5 min creates a uniform layer on the oxidized surface of the wafer. Hard baking in a vacuum oven at 260°C for 3 h completes the imidization reaction. Application of a spin-on-glass (SOG; Filmtronics) material by spin-coating at 1500 rpm for 30 s, and thermal curing on a hotplate at 210°C for 1 min yields a 500 nm-thick SiO_2 dielectric layer on top of polyimide layer. Electron-beam evaporation defines a bilayer of titanium (10 nm) and gold (120 nm). Photolithographic patterning of this bilayer involves spin-coating photoresist (AZ5214) at 3000 rpm for 40 s, soft baking at 110°C for 1 min, UV exposing for 7 s, and developing (AZ 300 MIF) for 2 min. Sequential immersion in gold and buffered oxide etchants removed the Au and Ti, respectively, to define serpentine traces in Au/Ti. Washing in acetone removes the residual photoresist. The final step applies a uniform coating of SiO_2 using the same SOG process described above.

4.2 | Substrates and Encapsulants

(1) Polyanhydride: Preparation of the polymer substrate begins by introducing a polyanhydride (PA) precursor into a PDMS mold via capillary action. UV curing at 365 nm (590 μW/cm^2) for 5 min forms a freestanding PA film. Mixing 4-pentenoic anhydride (4PA), 1,3,5-triallyl-1,3,5-triazine-2,4,6(1H,3H,5H)-trione (TTT), and 1,4-butanedithiol (BDT) at a molar ratio of 1:4:7, followed by vortexing, yields a homogeneous PA precursor solution. Physical delamination of the overlying PI layer and patterned Au interconnects from the silicon wafer enables transfer onto the PA film. Reactive ion etching (RIE, SAMCO) in oxygen plasma for 6 min selectively removes the PI layer to define electrical contact pads. A two-step dry etching process using CF_4/O_2 plasma (2 min) and CF_4 plasma (3 min) eliminates residual PI and the underlying SiO_2 dielectric layer. Dispensing additional PA precursor between the device and a PDMS mold, followed by UV curing (365 nm, 590 μW/cm^2) for 10 min, completes the encapsulation. Removal of the mold produces a 250 μm-thick bioresorbable encapsulation layer, completing the final system. (2) Regenerated silk fibroin: A previously established protocol yields regenerated silk fibroin (RSF) [84]. Cutting *Bombyx mori* silk cocoons into small pieces and boiling them in 0.02 M sodium carbonate (Na_2CO_3) solution (Sigma-Aldrich) for 30 min removes the sericin. Degummed fibers undergo drying and subsequent dissolution in 9.3 M lithium bromide (LiBr) solution (Sigma-Aldrich) at 60°C for 1 h, producing a silk fibroin solution. The process continues by transferring the solution into dialysis tubing (Fisherbrand, MWCO 3.5 K), followed by dialysis against deionized water for 3 days with at least five separate water exchanges, which yields purified silk fibroin. A centrifuge operating at 11,400 g for 20 min at 4°C clarifies the solution. The clarified solution then undergoes overnight freezing at –80°C, and vacuum drying using a lyophilizer (Labconco, –80°C, 0.006 bar) produces dried RSF. A ball mill grinds the dried RSF into a fine powder. Dissolution of the powder in hexafluoro-2-propanol (HFIP) results in a 4 wt.% solution. The formulation incorporates glycerol as a plasticizer in concentrations ranging from 0% up to 25% of the total silk mass, with 5% intervals, to improve flexibility and processability. A volume of 300 μL of the prepared solution per square inch coats a wafer bearing a predeposited Au electrode, and the film dries overnight under ambient conditions. The dried RSF film with the Au electrode detaches cleanly from the substrate, completing the film preparation. The subsequent steps, including PI etching and SiO_2 backend processing, follow the procedures described in the *"Substrates and encapsulants"* section, with RSF replacing PA as the encapsulant material.

4.3 | Components for Wireless Power

Laser-cut Mo foils (15-μm thick; Goodfellow) defined the R_x coils together with the extension and cuff electrodes. Films of PU and PA served as substrates with sufficient adhesion to

prevent displacement of the foils during laser cutting. The R_x coils adopted a bilayer layout with 11 turns per layer, each with a line width and spacing of 100 μm. A PIN (p-type–intrinsic–n-type) diode enabled efficient rectification, and a voltage-regulating diode (onsemi, 4.3 V) limited the output delivered to the heater. The use of a biodegradable W/wax conductive paste formed the electrical connections between the coil, via regions, and diode, thereby finalizing the R_x coil. The voltage-regulating diode joined with the contact pads of the extension electrode of wireless R_x coil with solder paste (CHIPQUIK, TS391AX10) applied using a hot air gun at 285°C. Details of the component's configuration are in Figure S15.

4.4 | Multiphysics Simulation of Mechanical and Thermal Behavior-Mechanical Deformation

The simulation uses ABAQUS (v. 2023) to analyze mechanical deformations during device operation and placement, including stretching, twisting, and bending, and determines the stretchability limits along with the bending and twisting thresholds at which the gold (Au) serpentine interconnects remain below the yield strain ($\varepsilon = 0.3\%$), thereby ensuring fully reversible elastic deformation. The wrapping-induced bending model ensures conformal contact between the device and a fixed cylindrical surface (radius = 1.5 mm), representing the geometry of a peripheral nerve. The model represents the ultrathin Au layers (120 nm) as shell surfaces and meshes them with composite shell elements (S4R), while it represents the 3D bioresorbable polyanhydride (PA) encapsulation with plasticized silk fibroin using 8-node linear hexahedral elements with reduced integration (C3D8R). A high-resolution mesh of approximately 1.15×10^6 elements captures critical stress gradients, with a minimum element size of 25 μm applied to the serpentine width to ensure convergence for all cases. The material definitions specify the elastic modulus (E) and Poisson's ratio (ν) as $E_{Au} = 78$ GPa and $\nu_{Au} = 0.44$ for gold, and $E_{PA} = 10$ MPa and $\nu_{PA} = 0.475$ for PA encapsulation, and $E_{Silk} = 4$ GPa (125 MPa for plasticized-silk), and $\nu_{Silk} = 0.33$ for the silk encapsulation.

4.5 | Transient Thermal Analysis

The meshed geometry of the wrapped thermal block enters COMSOL Multiphysics (version 6.2) from ABAQUS and enables three-dimensional transient thermal analysis, quantifying thermal gradients and overall temperature changes in both the sensor and the underlying nerve. The time-dependent form of the heat transfer equation appears as:

$$\rho C_P \frac{\partial T}{\partial t} + \nabla \cdot (-k \nabla T) = Q \tag{1}$$

where ρ is the material density, C_P is the specific heat capacity, k is the thermal conductivity, T is the temperature, t is time, Q is an internal heat generation term, and ∇ is the gradient operator. The transient thermal response of the device–nerve system arises from well-defined initial and boundary conditions. At $t = 0$ s, the computational domain maintains a uniform initial temperature ($T_0 = 25$°C). The heater serpentine traces follow a Dirichlet boundary condition, fixing the steady-state temperature at T_{heater} based on the input current I_{input} to mimic continuous Joule heating during device operation in a 37°C physiological environment. The complete finite element mesh consists of 2 530 341 domain elements, 102 218 boundary elements, and 36 820 edge elements, which ensure sufficient spatial resolution of steep temperature gradients within both the serpentine heater and the underlying nerve. A minimum time step of 2.5 s resolves the transient thermal evolution in regions of high thermal flux near the edges of the serpentine interconnects. To approximate heat loss to the surrounding environment, the exterior surfaces follow a convective boundary condition with a low heat transfer coefficient ($h = 2$ W m^{-2} K^{-1}), representative of stagnant biofluid conditions in the hydrogel environment. The interface between the nerve and the thermal block enforces a thermal continuity condition to ensure temperature continuity at the contact surface ($T_{PA} = T_{nerve}$). The density (ρ), specific heat capacity (C_P), and thermal conductivity (k) are 1000 kg m^{-3}, 3600 J kg^{-1} K^{-1}, and 0.35 W m^{-1} K for the nerve; 1000 kg m^{-3}, 1670 J kg^{-1} K^{-1}, and 0.63 W m^{-1} K^{-1} for the PA encapsulation; and 19300 kg m^{-3}, 129 J kg^{-1} K^{-1}, and 317 W m^{-1} K^{-1} for gold.

4.6 | Theoretical Resistance Changes from Au Trace Deformation

Bending-induced strain for a linear geometric structure can be calculated analytically as:

$$\varepsilon_b = \frac{y}{\rho} \tag{2}$$

Where ρ is the radius of the neutral axis and y is the distance from the neutral axis to the point of interest. In this range, curvatures of 0.01–1 mm^{-1} map to radii of curvature spanning 100 to 1 mm. The point of interest, y, is taken as half the width of the gold trace (0.006 mm), yielding a strain range of 0.00006–0.006.

The strain is related to the change in resistance as:

$$\frac{\Delta R}{R_0} = GF\varepsilon_b \tag{3}$$

Where GF is the gauge factor. However, for a serpentine geometry rather than a linear structure, the intrinsic strain direction does not necessarily align with the bending direction, which can be described by the average strain

$$\varepsilon_{av} = \frac{y}{\rho}\left(\frac{1}{L}\int_0^L \cos^2\theta ds\right) \tag{4}$$

Where the integral term $\frac{1}{L}\int_0^L \cos^2\theta ds$ captures the nonlinear geometric effects of the serpentine, with values ranging from 0.05 to 0.2 for the device design. Then, for this design, the approximate resistance change can be approximated as

$$\frac{\Delta R}{R_0} = GF\varepsilon_{av} = GF\frac{0.0006}{10}(0.2) = GF\,(0.000012)$$
$$= 100\,(0.000012) = 0.0012 \tag{5}$$

4.7 | Characterization-Hydrogel Environment Setup for Thermal Performance Evaluation

Thermal characterization uses a hydrogel environment designed to replicate tissue-mimicking conditions. Immersion in an agarose-based hydrogel (0.5 wt.%, Sigma Aldrich) bath maintains the device at 37°C ± 0.2°C using a hot plate. A DC power supply delivers controlled currents to the integrated heater traces, and an infrared (IR) camera (FLIR A600, Teledyne FLIR LLC) monitors the spatiotemporal temperature distribution across the device surface. The system records IR data for analysis on a connected laptop to extract thermal profiles under varying electrical inputs.

4.8 | Electrothermal Characterization

Thermal performance assessment system begins with IR thermography under controlled current input conditions. Stepwise increases in current apply with a DC-regulated power supply (TP300ST, TekPower) activated the resistive heating elements. An IR camera captures the corresponding surface temperatures. Repeated heating and cooling cycles provide insights into thermal stability and reversibility. Heat distribution profiles, analyzed at steady-state conditions, confirm localized thermal effects.

4.9 | Mechanical Characterization

The mechanical durability measurements include repetitive cycles of uniaxial bending and twisting. Bending occurs at a rate of 10 mm/s and twisting proceeds at 30°/s in repeated cycles. LabVIEW software with a resistance calculation algorithm, a Source Meter (Keithley 2602, Tektronix), and a data acquisition system (DAQ) monitor changes in sensor resistance during cyclic mechanical loading. IR thermography also evaluates the thermal performance of the heater under bending and twisting conditions.

4.10 | Fourier-Transform Infrared Spectroscopy (FTIR) Analysis

Analyzing the degree of crystallinity in silk-based devices with varying glycerol content uses attenuated total reflectance-Fourier transform infrared spectroscopy (ATR-FTIR; Nicolet Nexus 870, Thermo Scientific). The system acquires all FTIR curves over the range of 400–4000 cm^{-1} at a resolution of 4 cm^{-1}, averaging 32 scans per sample. Gaussian peak deconvolution over the amide I and II regions (1700–1450 cm^{-1}) employs a secondary derivative method. The six primary peaks include: 1520–1530 cm^{-1} (β-sheet), 1545 cm^{-1} (random coil/helix), 1620 cm^{-1} (β-sheet), 1640–1655 cm^{-1} (random coil/helix), 1685 cm^{-1} (β-turn), and 1698–1700 cm^{-1} (β-sheet).

4.11 | Tests for Dissolution of Devices

The tests begin with immersion of devices in plastic well chambers (37 mm diameter) filled with 10 mL of 1×PBS (pH7.4) at 37°C. LabVIEW software and a source meter record the resistance properties of the devices every other day for 14 days. Replacing PBS between measurements minimizes interference from residual reaction species.

4.12 | In Vitro Quantitative Degradation Kinetics

The protocol begins with measuring the initial mass of SF-based devices with different β-sheet crystallinity. The samples undergo incubation at 37°C in 1× PBS (pH 7.4), with or without chymotrypsin (1 or 40 U/mL). At predetermined time points (1, 2, 4, 7, and 14 days), the procedure retrieves the samples, rinses them in deionized water, and dries them in a convection oven (∼75°C) before performing the final weighing. The remaining mass converts to residual mass ratio (%) for quantitative analysis of degradation kinetics.

4.13 | Wireless Operation

A commercial RF system (NeuroLux, Inc., Evanston, IL) wirelessly delivers power to the device (Figure S15). An oscilloscope (TBS1032B; Tektronix) measures the output voltage transmitted to the device as a function of the supplied wireless power. The harvesting circuit employs a half-bridge rectifier with a voltage-regulating diode (onsemi., 4.3 V) to limit the input voltage and prevent overheating of the heater, thereby minimizing tissue damage and electrode corrosion. The experiment adjusts the applied power and duration for heater activation demonstrations. An IR camera (FLIR A600, Teledyne FLIR LLC) monitors the top surface temperature of the device during operation. The detailed experimental setup appears in Figure S15, Supporting Information.

4.14 | In Vivo Experimental Setup and Electrophysiological Evaluation-Preparation for Surgery

Animal studies adhere to protocols approved by the Institutional Animal Care and Use Committees at Washington University in St. Louis and conform to the *Guide for the Care and Use of Laboratory Animals*. Surgical procedures begin with anesthetizing the rats using 5% isoflurane/95% oxygen for induction and 2% isoflurane/98% oxygen for maintenance, administered via inhalation. Preparation of the animals includes shaving the fur, applying isopropanol and Betadine to the right leg, and introducing analgesia through a subcutaneous injection of Buprenorphine SR (1 mg/mL; ZooPharm) at a dose of 1.2 mg/kg. The surgery begins with an incision parallel to the right femur to split the gluteal muscles and the biceps femoris. Blunt dissection mobilizes the sciatic nerve and the branch of the peroneal nerve.

4.15 | Electrophysiology Measurements

The PA-based devices wrap circumferentially around the sciatic nerve. The bipolar stimulating electrode positions 3 mm proximal to the device, and the recording cuff (MicroProbes) sits 3 mm distal around the peroneal branch. A DC power supply (TP300ST, TekPower) delivers current to the thermal actuator. A source meter (Keithley 2602, Tektronix) applies a constant current of

100 μA to the thermistor and measures the resistance. A custom stimulation system and data acquisition software (Red Rock Laboratories) generate stimulation pulses (amplitude, 1 mV; burst width, 0.3 s; duration, 50 μs). The system amplifies and records CNAP signals every minute over a 5 min period. Thermal accumulation induces a complete nerve conduction block, and passive cooling for over 5 min enables recovery of neural activity.

Acknowledgements

J.P., H.-Y.A., M.S., T.K., and Y.Z. contributed equally to this work. This work made use of the NUFAB facility of Northwestern University's NUANCE Center, which has received support from the SHyNE Resource (NSF ECCS-2025633), the IIN, and Northwestern's MRSEC program (NSF DMR-2308691). This research was supported by the National Research Foundation of Korea (NRF) grant funded by the Korea government (MSIT) (RS-2024-00358488 and RS-2023-00218812) and by the Korea government (MOE) (NO.2120241415340). R.R.M. acknowledges support from the Rice University Academy of Fellows. R.A. acknowledges seed funding from the Rice University ENRICH Office and the ASME Haythornthwaite Foundation Research Initiation Grant from the Applied Mechanics Division (AMD).

Conflicts of Interest

The authors declare no conflict of interest.

Data Availability Statement

The data that supports the findings of this study are available from the corresponding author upon reasonable request.

References

1. L. Colloca, T. Ludman, D. Bouhassira, et al., "Neuropathic Pain," *Nature Reviews Disease Primers* 3 (2017): 17002.

2. N. Volkow, H. Benveniste, and A. T. McLellan, "Use and Misuse of Opioids in Chronic Pain," *Annual Review of Medicine* 69 (2018): 451–465.

3. C. S. Florence, C. Zhou, F. Luo, and L. Xu, "The Economic Burden of Prescription Opioid Overdose, Abuse, and Dependence in the United States, 2013," *Medical Care* 54 (2016): 901–906.

4. M. T. Flavin, J. A. Foppiani, M. A. Paul, et al., "Bioelectronics for Targeted Pain Management," *Nature Reviews Electrical Engineering* 2 (2025): 407–424.

5. Y. Zeng, C. Gong, G. Lu, et al., "A Programmable and Self-adaptive Ultrasonic Wireless Implant for Personalized Chronic Pain Management," *Nature Electronics* 8 (2025): 437–449.

6. J. C. Chen, P. Kan, Z. Yu, et al., "A Wireless Millimetric Magnetoelectric Implant for the Endovascular Stimulation of Peripheral Nerves," *Nature Biomedical Engineering* 6 (2022): 706–716.

7. H. Beltran-Alacreu, D. Serrano-Muñoz, D. Martin-Caro Alvarez, J. J. Fernández-Pérez, J. Gómez-Soriano, and J. Avendaño-Coy, "Percutaneous versus Transcutaneous Electrical Nerve Stimulation for the Treatment of Musculoskeletal Pain. A Systematic Review and Meta-analysis," *Pain Medicine* 23 (2022): 1387–1400.

8. M. I. Johnson, C. A. Paley, G. Jones, M. R. Mulvey, and P. G. Wittkopf, "Efficacy and Safety of Transcutaneous Electrical Nerve Stimulation (TENS) for Acute and Chronic Pain in Adults: A Systematic Review and Meta-analysis of 381 Studies (the meta-TENS study)," *BMJ Open* 12 (2022): 051073.

9. A. G. El-Sayed, P. F. White, H. E. Ahmed, M. A. Hamza, W. F. Craig, and C. E. Noe, "Percutaneous Electrical Nerve Stimulation: An Alternative to TENS in the Management of Sciatica," *Pain* 83 (1999): 193.

10. C. E. Larson and E. Meng, "A Review for the Peripheral Nerve Interface Designer," *Journal of Neuroscience Methods* 332 (2020): 108523.

11. A. Carnicer-Lombarte, A. J. Boys, A. Güemes, et al., "Ultraconformable Cuff Implants for Long-term Bidirectional Interfacing of Peripheral Nerves at Sub-nerve Resolutions," *Nature Communications* 15 (2024): 7523.

12. J. M. Henderson, "Peripheral Nerve Stimulation for Chronic Pain," *Current Pain and Headache Reports* 12 (2008): 28–31.

13. B. Albright-Trainer, T. Phan, R. J. Trainer, et al., "Peripheral Nerve Stimulation for the Management of Acute and Subacute Post-amputation Pain: A Randomized, Controlled Feasibility Trial," *Pain Management* 12 (2022): 357–369.

14. P. F. White, W. F. Craig, A. S. Vakharia, E. A. Ghoname, H. E. Ahmed, and M. A. Hamza, "Percutaneous Neuromodulation Therapy: Does the Location of Electrical Stimulation Effect the Acute Analgesic Response?," *Anesthesia & Analgesia* 91 (2000): 949–954.

15. A. Carnicer-Lombarte, S.-T. Chen, G. G. Malliaras, and D. G. Barone, "Foreign Body Reaction to Implanted Biomaterials and Its Impact in Nerve Neuroprosthetics," *Frontiers in Bioengineering and Biotechnology* 9 (2021): 622524.

16. M. B. Christensen and P. A. Tresco, "The Foreign Body Response and Morphometric Changes Associated With Mesh-style Peripheral Nerve Cuffs," *Acta Biomaterialia* 67 (2018): 79–86.

17. J. E. Pope, T. R. Deer, D. Sayed, et al., "The American Society of Pain and Neuroscience (ASPN) Guidelines and Consensus on the Definition, Current Evidence, Clinical Use and Future Applications for Physiologic Closed-Loop Controlled Neuromodulation in Chronic Pain: A NEURON Group Project," *Journal of Pain Research* 18 (2025): 531–551.

18. J. Wang and Z. S. Chen, "Closed-loop Neural Interfaces for Pain: Where Do We Stand?," *Cell Reports Medicine* 5 (2024): 101662.

19. G. Lee, E. Ray, H.-J. Yoon, et al., "A Bioresorbable Peripheral Nerve Stimulator For Electronic Pain Block," *Science Advances* 8 (2022): abp9169.

20. H.-Y. Ahn, J. B. Walters, R. Avila, et al., "Bioresorbable, Wireless Dual Stimulator for Peripheral Nerve Regeneration," *Nature Communications* 16 (2025): 4752.

21. D.-M. Lee, M. Kang, I. Hyun, et al., "An On-Demand Bioresorbable Neurostimulator," *Nature Communications* 14 (2023): 7315.

22. Y. S. Choi, Y.-Y. Hsueh, J. Koo, et al., "Stretchable, Dynamic Covalent Polymers for Soft, Long-lived Bioresorbable Electronic Stimulators Designed to Facilitate Neuromuscular Regeneration," *Nature Communications* 11 (2020): 5990.

23. A. J. Bahnick, C. S. Dziewior, Y. Li, et al., "Controlled Transdermal Delivery of Dexamethasone for Pain Management via Photochemically 3D-Printed Bioresorbable Microneedle Arrays," *Advanced Healthcare Materials* 13 (2024): 2402113.

24. K. Yu, X. Niu, and B. He, "Neuromodulation Management of Chronic Neuropathic Pain in the central Nervous System," *Advanced Functional Materials* 30 (2020): 1908999.

25. A. R. Ward, "Electrical Stimulation Using Kilohertz-frequency Alternating Current," *Physical Therapy* 89 (2009): 181–190.

26. N. Bhadra, T. L. Vrabec, N. Bhadra, and K. L. Kilgore, "Reversible Conduction Block in Peripheral Nerve Using Electrical Waveforms," *Bioelectronics in Medicine* 1 (2018): 39–54.

27. G. C. McConnell, H. D. Rees, A. I. Levey, C.-A. Gutekunst, R. E. Gross, and R. V. Bellamkonda, "Implanted Neural Electrodes Cause Chronic, Local Inflammation That Is Correlated With Local Neurodegeneration," *Journal of Neural Engineering* 6 (2009): 056003.

28. E. S. Boyden, "Optogenetics and the Future of Neuroscience," *Nature Neuroscience* 18 (2015): 1200–1201.

29. L. Li, L. Lu, Y. Ren, et al., "Colocalized, Bidirectional Optogenetic Modulations in Freely Behaving Mice With a Wireless Dual-color Optoelectronic Probe," *Nature Communications* 13 (2022): 839.

30. B. E. Maimon, K. Sparks, S. Srinivasan, A. N. Zorzos, and H. M. Herr, "Spectrally Distinct Channelrhodopsins for Two-colour Optogenetic Peripheral Nerve Stimulation," *Nature Biomedical Engineering* 2 (2018): 485–496.

31. S. I. Park, D. S. Brenner, G. Shin, et al., "Soft, Stretchable, Fully Implantable Miniaturized Optoelectronic Systems for Wireless Optogenetics," *Nature Biotechnology* 33 (2015): 1280–1286.

32. M. Cho, J. K. Han, J. Suh, et al., "Fully Bioresorbable Hybrid Optoelectronic Neural Implant System for Simultaneous Electrophysiological Recording and Optogenetic Stimulation," *Nature Communications* 15 (2024): 2000.

33. X. Liu, S. Rao, W. Chen, et al., "Fatigue-resistant Hydrogel Optical Fibers Enable Peripheral Nerve Optogenetics During Locomotion," *Nature Methods* 20 (2023): 1802–1809.

34. M. A. Fishman, A. M. Scherer, A. M. Katsarakes, L. Larson, and P. S. Kim, "Temperature-mediated Nerve Blocks in the Treatment of Pain," *Current Pain and Headache Reports* 25 (2021): 60.

35. H. Tao, S.-W. Hwang, B. Marelli, et al., "Silk-based Resorbable Electronic Devices for Remotely Controlled Therapy and in Vivo Infection Abatement," *Proceedings of the National Academy of Sciences* 111 (2014): 17385–17389.

36. J. T. Reeder, Z. Xie, Q. Yang, et al., "Soft, Bioresorbable Coolers for Reversible Conduction Block of Peripheral Nerves," *Science* 377 (2022): 109–115.

37. J. Kim, J. S. Lee, S. Noh, et al., "Cellular Level Cryo-neuromodulation Using Rapid and Localized Cooling Device Combined With Microelectrode Array," *Biosensors and Bioelectronics* 277 (2025): 117257.

38. L. Zhang, S. Xing, H. Yin, et al., "Skin-inspired, Sensory Robots for Electronic Implants," *Nature Communications* 15 (2024): 4777.

39. S. Hong, H. Lee, J. Lee, et al., "Highly Stretchable and Transparent Metal Nanowire Heater for Wearable Electronics Applications," *Advanced Materials* 27 (2015): 4744–4751.

40. M. Seong, I. Hwang, S. Park, et al., "Enhanced Thermal Transport Across Self-Interfacing van der Waals Contacts in Flexible Thermal Devices," *Advanced Functional Materials* 31 (2021): 2107023.

41. Á. C. Horváth, S. Borbély, Ö. C. Boros, et al., "Infrared Neural Stimulation and Inhibition Using an Implantable Silicon Photonic Microdevice," *Microsystems & Nanoengineering* 6 (2020): 44.

42. J. Zhuo, C. E. Weidrick, Y. Liu, et al., "Selective Infrared Neural Inhibition Can be Reproduced by Resistive Heating," *Neuromodulation: Technology at the Neural Interface* 26 (2023): 1757–1771.

43. Y. Wang, X. Wang, J. Shi, R. Zhu, J. Zhang, and Z. Zhang, "Flexible Silk Fibroin Films Modified by Genipin and Glycerol," *RSC Advances* 5 (2015): 101362–101369.

44. J. Viventi, D.-H. Kim, L. Vigeland, et al., "Flexible, Foldable, Actively Multiplexed, High-density Electrode Array for Mapping Brain Activity in Vivo," *Nature Neuroscience* 14 (2011): 1599–1605.

45. N. Obidin, F. Tasnim, and C. Dagdeviren, "The Future of Neuroimplantable Devices: A Materials Science and Regulatory Perspective," *Advanced Materials* 32 (2020): 1901482.

46. Y. S. Choi, J. Koo, Y. J. Lee, et al., "Biodegradable Polyanhydrides as Encapsulation Layers for Transient Electronics," *Advanced Functional Materials* 30 (2020): 2000941.

47. D.-H. Kim, J. Viventi, J. J. Amsden, et al., "Dissolvable Films of Silk Fibroin for Ultrathin Conformal Bio-integrated Electronics," *Nature Materials* 9 (2010): 511–517.

48. H. Tao, J. M. Kainerstorfer, S. M. Siebert, et al., "Implantable, Multifunctional, Bioresorbable Optics," *Proceedings of the National Academy of Sciences* 109 (2012): 19584–19589.

49. D.-L. Wen, D.-H. Sun, P. Huang, et al., "Recent Progress in Silk Fibroin-based Flexible Electronics," *Microsystems & Nanoengineering* 7 (2021): 35.

50. Y. Wang, X. Feng, and X. Chen, "Autonomous Bioelectronic Devices Based on Silk Fibroin," *Advanced Materials* 37 (2025): 2500073.

51. A. Bucciarelli and A. Motta, "Use of Bombyx mori Silk Fibroin in Tissue Engineering: From Cocoons to Medical Devices, Challenges, and Future Perspectives," *Biomaterials Advances* 139 (2022): 212982.

52. S. K. Kang, S. W. Hwang, H. Cheng, et al., "Dissolution Behaviors and Applications of Silicon Oxides and Nitrides in Transient Electronics," *Advanced Functional Materials* 24 (2014): 4427–4434.

53. Y. K. Lee, K. J. Yu, Y. Kim, et al., "Kinetics and Chemistry of Hydrolysis of Ultrathin, Thermally Grown Layers of Silicon Oxide as Biofluid Barriers in Flexible Electronic Systems," *ACS Applied Materials & Interfaces* 9 (2017): 42633–42638.

54. Y. Zhang, G. Lee, S. Li, Z. Hu, K. Zhao, and J. A. Rogers, "Advances in Bioresorbable Materials and Electronics," *Chemical Reviews* 123 (2023): 11722–11773.

55. S.-W. Hwang, J.-K. Song, X. Huang, et al., "High-Performance Biodegradable/Transient Electronics on Biodegradable Polymers," *Advanced Materials* 26 (2014): 3905–3911.

56. A. E. Thurber, F. G. Omenetto, and D. L. Kaplan, "In Vivo Bioresponses To Silk Proteins," *Biomaterials* 71 (2015): 145–157.

57. C. Guo, C. Li, H. V. Vu, et al., "Thermoplastic Moulding of Regenerated Silk," *Nature Materials* 19 (2020): 102–108.

58. Y. Wang, J. Wu, E. J. Hartzell, et al., "Living Plastics From Plasticizer-Assisted Thermal Molding of Silk Protein," *Nature Communications* 16 (2025): 52.

59. G. Guidetti, L. d'Amone, T. Kim, et al., "Silk Materials at the Convergence of Science, Sustainability, Healthcare, and Technology," *Applied Physics Reviews* 9 (2022): 011302.

60. T. Kim, B. J. Kim, G. E. Bonacchini, N. A. Ostrovsky-Snider, and F. G. Omenetto, "Silk Fibroin as a Surfactant for Water-based Nanofabrication," *Nature Nanotechnology* 19 (2024): 1514–1520.

61. J. K. Sahoo, O. Hasturk, T. Falcucci, and D. L. Kaplan, "Silk Chemistry and Biomedical Material Designs," *Nature Reviews Chemistry* 7 (2023): 302–318.

62. Z. Zhu, S. Ling, J. Yeo, et al., "High-Strength, Durable All-Silk Fibroin Hydrogels With Versatile Processability Toward Multifunctional Applications," *Advanced Functional Materials* 28 (2018): 1704757.

63. Y. Wang, Z. Zheng, Q. Cheng, D. L. Kaplan, G. Li, and X. Wang, "Ductility and Porosity of Silk Fibroin Films by Blending With Glycerol/Polyethylene Glycol and Adjusting the Drying Temperature," *ACS Biomaterials Science & Engineering* 6 (2020): 1176–1185.

64. S. Lu, X. Wang, Q. Lu, et al., "Insoluble and Flexible Silk Films Containing Glycerol," *Biomacromolecules* 11 (2010): 143–150.

65. H. Lyu, Z. Sun, Y. Liu, X. Yu, and C. Guo, "Processing-Structure-Properties Relationships of Glycerol-Plasticized Silk Films," *Molecules* 27 (2022): 1339.

66. H. H. Tuson, G. K. Auer, L. D. Renner, et al., "Measuring the Stiffness of Bacterial Cells From Growth Rates in Hydrogels of Tunable Elasticity," *Molecular Microbiology* 84 (2012): 874–891.

67. M. Zhang, Z. Che, J. Chen, et al., "Experimental Determination of Thermal Conductivity of Water– Agar Gel at Different Concentrations and Temperatures," *Journal of Chemical & Engineering Data* 56 (2011): 859–864.

68. M. A. Fishman, A. Chitneni, A. Abd-Elsayed, et al., "Drug-Free Noninvasive Thermal Nerve Block: Validation of Sham Devices," *Brain Sciences* 13 (2023): 1718.

69. J. S. Brodkey, Y. Miyazaki, F. R. Ervin, and V. H. Mark, "Reversible Heat Lesions With Radiofrequency Current," *Journal of Neurosurgery* 21 (1964): 49–53.

70. A. Oliva and J. Lugo, "Measurement of the Temperature Coefficient of Resistance in Metallic Films With Nano-thickness," *International Journal of Thermophysics* 37 (2016): 35.

71. N. Lu and S. Yang, "Mechanics for Stretchable Sensors," *Current Opinion in Solid State and Materials Science* 19 (2015): 149–159.

72. S. M. Won, H.-S. Kim, N. Lu, et al., "Piezoresistive Strain Sensors and Multiplexed Arrays Using Assemblies of Single-crystalline Silicon Nanoribbons on Plastic Substrates," *IEEE Transactions on Electron Devices* 58 (2011): 4074–4078.

73. K. H. Jung, J. Hyun, M. W. Jeong, et al., "A biocompatible elastomeric organic transistor for implantable electronics," *Nature Electronics* 8 (2025): 831–843.

74. R. S. Dyer and W. K. Boyes, "Hypothermia and Chloropent Anesthesia Differentially Affect the Flash Evoked Potentials of Hooded Rats," *Brain Research Bulletin* 10 (1983): 825–831.

75. B. Redfors, Y. Shao, and E. Omerovic, "Influence of Anesthetic Agent, Depth of Anesthesia and Body Temperature on Cardiovascular Functional Parameters in the Rat," *Laboratory Animals* 48 (2014): 6–14.

76. J. Hoogeveen, D. Troost, A. Van Der Kracht, J. Wondergem, J. Haveman, and D. G. Gonzalez, "Ultrastructural Changes in the Rat Sciatic Nerve After Local Hyperthermia," *International Journal of Hyperthermia* 9 (1993): 723–730.

77. Z. Zhang, T. D. Lyon, B. T. Kadow, et al., "Conduction block of mammalian myelinated nerve by local cooling to 15–30°C After a brief heating," *Journal of Neurophysiology* 115 (2016): 1436–1445.

78. Z. Vujaskovic, S. M. Gillette, B. Powers, et al., "Effects of Intraoperative Hyperthermia on Peripheral Nerves: Neurological and Electrophysiological Studies," *International Journal of Hyperthermia* 10 (1994): 41–49.

79. G. C. Van Rhoon, T. Samaras, P. S. Yarmolenko, M. W. Dewhirst, E. Neufeld, and N. Kuster, "CEM43° C Thermal Dose Thresholds: A Potential Guide for Magnetic Resonance Radiofrequency Exposure Levels?," *European Radiology* 23 (2013): 2215–2227.

80. P. S. Yarmolenko, E. J. Moon, C. Landon, et al., "Thresholds for Thermal Damage to Normal Tissues: An Update," *International Journal of Hyperthermia* 27 (2011): 320–343.

81. W. Ouyang, W. Lu, Y. Zhang, et al., "A Wireless and Battery-less Implant for Multimodal Closed-loop Neuromodulation in Small Animals," *Nature Biomedical Engineering* 7 (2023): 1252–1269.

82. Y. Wu, M. Wu, A. Vázquez-Guardado, et al., "Wireless Multi-lateral Optofluidic Microsystems for Real-time Programmable Optogenetics and Photopharmacology," *Nature Communications* 13 (2022): 5571.

83. P. Gutruf, V. Krishnamurthi, A. Vázquez-Guardado, et al., "Fully Implantable Optoelectronic Systems for Battery-free, Multimodal Operation in Neuroscience Research," *Nature Electronics* 1 (2018): 652–660.

84. D. N. Rockwood, R. C. Preda, T. Yücel, X. Wang, M. L. Lovett, and D. L. Kaplan, "Materials Fabrication From Bombyx mori Silk Fibroin," *Nature Protocols* 6 (2011): 1612–1631.

Supporting Information

Additional supporting information can be found online in the Supporting Information section.

Supporting File: adfm73540-sup-0001-SuppMat.docx